

# DEVELOPING A TOOL FOR THE SPECTRAL ANALYSIS OF METAL-POOR RGB STARS WITH X-SHOOTER

*Klein Onderzoek* thesis

LEON (L.M.P.V.) BOSCHMAN

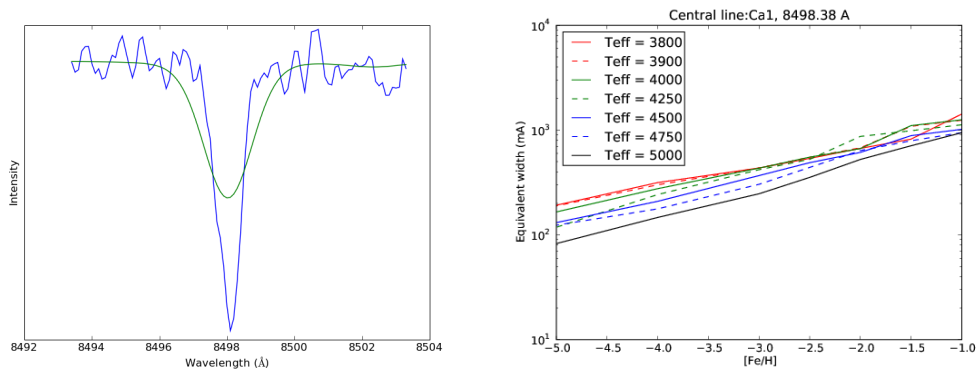
Supervisors: Eline Tolstoy, Else Starkenburg

*Kapteyn Astronomical Institute, University of Groningen*

February 16, 2011

## Abstract

In this project we used synthetic spectra to study the behavior of absorption lines from metal-poor RGB stars in the X-shooter spectrograph. Using one synthetic spectrum, we searched for feasible absorption lines in the UB and the VRI bands that would be detectable with X-shooter. Then we calculated spectra for RGB stars with different metallicities and effective temperatures, creating a grid of model spectra. With these spectra, we studied the dependence of the equivalent width of every absorption line on the metallicity and temperature. Additionally, we checked for blending with other stellar absorption lines and with telluric absorption lines as well. The result is a table of feasible absorption lines with a description of the dependence of the equivalent width on metallicity and temperature, together with blending warnings. This can be a useful tool when studying spectra of metal-poor RGB stars with X-shooter.



<b>1</b>	<b>Scientific Motivation</b>	<b>2</b>
<b>2</b>	<b>Background</b>	<b>5</b>
2.1	Absorption lines . . . . .	5
2.1.1	Line broadening . . . . .	5
2.1.2	Measuring absorption lines . . . . .	6
2.2	The modeling of the spectra . . . . .	7
2.2.1	Basic assumptions . . . . .	8
2.2.2	Model errors . . . . .	9
2.3	X-shooter . . . . .	10
<b>3</b>	<b>Method</b>	<b>12</b>
<b>4</b>	<b>Results</b>	<b>15</b>
<b>5</b>	<b>Discussion</b>	<b>20</b>
5.1	Sources of Error . . . . .	20
5.1.1	Errors in Creating Synthetic Spectra . . . . .	20
5.1.2	Equivalent Widths . . . . .	21
5.2	Results . . . . .	21
<b>6</b>	<b>Conclusions</b>	<b>22</b>
<b>7</b>	<b>Acknowledgements</b>	<b>23</b>

The primary goal of this project was to develop a tool to interpret spectra of individual stars taken with X-shooter, a new spectrograph at the Very Large Telescope with a large wavelength range. The stellar spectra obtained with this instrument allow us to gain detailed information about individual stars, such as chemical composition and physical parameters like temperature.

This information is obtained via the absorption lines one can find in a spectrum. Each element has its own collection of absorption (and sometimes emission) lines, and it is through these lines that we can infer numerous physical parameters of a star. For example, the depth of an absorption line, combined with the physical properties of the star, tells us how abundant the chemical species is that leads to the absorption line. The width of a line too can tell us several things about the physical conditions in a stellar atmosphere, like temperature and pressure. How this exactly works will be further explained in chapter 2.

We cannot measure these properties throughout the entire star. The processes of continuous absorption and emission only allow us to observe the outer layers of a star. However, these outer layers are of particular astronomical interest, because they do not change their chemical composition during the stellar lifetime (McWilliam, 1997).

This is in sharp contrast to the nucleus, which constantly alters its chemical abundance. That is done by the fusion of low-mass elements into higher-mass elements, e.g. C, N and O. During this process energy is produced, which is used to heat the star. The other consequence of this process is of course that the abundance of lower-mass elements, and particularly hydrogen decreases with time, while higher-mass elements become more abundant with time. The exact distribution of these elements depends on the mass of the star, e.g. Ivens et al. (2001). However, very high temperatures are necessary for nuclear fusion and therefore these processes only take place in the core of a star.

We are primarily interested in red giant branch (RGB) stars, for reasons that will be explained shortly. For these RGB stars, we make the assumption that there has been no substantial mixing of the core and the outer layers of the star. This assumption is believed to be very close to reality for the RGB stars studied in this project. Because there is no mixing of the core and the outer layers, the chemical composition of the stellar atmosphere should be the same as it was at the time the star was formed. It

is therefore a unique probe of the interstellar medium (ISM) from which the star was formed. So by studying the atmospheres of stars, we can study the ISM back at the time when the star was formed. If we extend our research to a large number of stars of different ages in the same region, it is possible to reconstruct the chemical composition of the ISM in a galaxy at different ages. This makes it possible to obtain the chemical history of a certain region or a whole galaxy, e.g. McWilliam (1997).

The chemical composition of the ISM in a galaxy can strongly influence the star formation rate in that region. The presence of metals makes it easier to cool the gas and efficient cooling is a prerequisite for star formation (Tielens, 2005; Salaris and Cassisi, 2005). On the other hand, the number of stars also affects the chemical composition of the ISM. During their life, stars produce a variety of metals<sup>1</sup>. These metals are fed back into the ISM through stellar winds and supernovae. In stellar winds, gas from the outer layers of a star is blown into the ISM, carrying metals and gas into the surroundings. A supernova is an explosion at the end of a star's life in which it loses most of its mass. There are several types of supernovae with different mechanisms, but they have in common that they carry a substantial amount of the newly formed elements into the ISM, e.g. Pagel (1997). This causes an increase in the metallicity of the ISM, the so-called chemical enrichment.

If we combine metallicity observations with star formations histories that are deduced from color-magnitude diagrams of that same region, one can infer a chemical history of that region. These star formation and chemical histories can be used to study galaxy evolution, for example by studying very small galaxies, so-called dwarf spheroidals, that surround our own Galaxy (Tolstoy et al., 2009). These dwarf spheroidals allow us to study galaxy formation and evolution on small scales. Detailed information about dwarf spheroidals is obtained by observing the individual stars they are made of and especially the luminous red giant branch stars or the RGB-stars. These RGB-stars have several advantages over other stars. First, they are bright, which makes them good observing candidates. The other reason to target RGB-stars is that RGB populations consist of stars of all ages, except the very young ones ( $< 1$  Gyr). So by observing large samples of RGB-stars, one can sample stars of a large variety of ages, which is necessary to determine the full chemical enrichment history of a dwarf spheroidal.

In this project we produce an overview of absorption lines and their behavior, such as dependence on temperature and metallicity. This overview is produced for use with the X-shooter spectrograph and is focused primarily on metal poor RGB stars. Therefore, it provides a nice tool to perform a quick analysis of X-shooter spectra of these metal poor RGB-stars. A direct application would be to study the spectra of extremely metal-poor stars in the Sculptor dwarf galaxy. These stars are selected from a low-resolution Ca-triplet survey (Starkenburg et al., 2010) and a detailed chemical abundance study would allow us to look at the earliest phase of star formation in such a small galaxy. In september 2010, X-shooter spectra have been obtained of 7 of such extremely metal-poor stars.

The first step in the development of this tool is to calculate synthetic spectra and to search for absorption lines in these spectra. These calculations are based on the physical

---

<sup>1</sup>in astronomy, all elements heavier than He are called metals

conditions in the stellar atmosphere, where the lines are formed. Therefore, we have to know how lines are formed and how their shape is affected by the physical conditions in the stellar atmosphere. This will be explained in section 2.1, together with an explanation of how lines are measured. How we calculate the physical parameters in the stellar atmosphere is further explained in 2.2, where we discuss the modelling of stellar atmospheres. The technical details of X-shooter and their influence on the measurements will be discussed in section 2.3. RGB-stars come with a range of temperatures, pressures and metallicities. Obviously, it is not enough to study just one spectrum with a certain temperature etc. Therefore, we used an entire grid of stellar models to compute the corresponding spectra. The exact grid and the method of analyzing the data is further explained in chapter 3. The results of this analysis are presented in chapter 4 and a discussion about the results and their consequences will be given in chapter 5.

To be able to give a quantitative description of the behavior of absorption lines, one first needs to know how these spectral lines are formed and which variables influence them. First we will focus on how and where absorption lines arise, then the importance of the spectrometer is explained and lastly we will explain how spectral lines are influenced by temperature, metallicity and several other variables.

## 2.1 Absorption lines

Absorption lines are formed when a photon excites an atom or a molecule into a higher energy level. This can only be done when the photon energy matches the energy difference between two energy levels, so this imposes a fairly strict requirement on the photons that can be absorbed. The absorption profile resembles a delta-function, as described in equation (2.1):

$$f(\lambda) = \delta(\lambda - \lambda_0) \quad (2.1)$$

where  $\lambda$  represents the wavelength and  $\lambda_0$  the central wavelength of the transition.

### 2.1.1 Line broadening

This absorption line is then broadened by several mechanisms, which we will explain below. Each mechanism leads to different broadening profile. The first broadening mechanism is the natural broadening. When an atom is excited, it will fall back into its original ground state on a well defined timescale. This characteristic timescale, the natural decay rate, causes the excited state to have a finite lifetime. We use the Heisenberg uncertainty relation in equation (2.2) to establish that there is an uncertainty in the energy difference between the excited and the ground state.

$$\Delta E \Delta t \geq \frac{\hbar}{2} \quad (2.2)$$

This uncertainty  $\Delta E$  is inversely proportional to the lifetime of the excited state and causes the atom to have a small variation in its energy levels. Therefore, an absorption

line has a finite width instead of a zero width. This is called the natural linewidth and it creates a Lorentzian profile.

In addition to natural line broadening, absorption lines are also broadened by thermal Doppler effects. This phenomenon is caused by the thermal motions of the atoms along the line of sight. The thermal motions along this line of sight follow a gaussian distribution centered at  $v = v_*$ , the velocity of the star with respect to us. The width of this distribution increases with temperature, because atoms have higher velocities at higher temperatures. This is because the receding atoms absorb photons that are slightly redder, while the approaching atoms absorb photons that are slightly bluer, which causes the absorption line profile to be broadened.

A third effect is pressure broadening, which also has to be taken into account. It bears a resemblance to the natural line broadening, in the sense that it is also caused by the finite lifetime of excited states. The key difference involves the way in which the excited states are depopulated. The natural linewidth finds its origin in spontaneous emission, whereas pressure broadening is caused by the collisionally stimulated depopulation of the excited state.

In this case, the lifetime of the excited state, and thus the line broadening, depends on the number of depopulating collisions per unit time. This number depends strongly on the temperature and the pressure of the gas in which the absorption lines are formed. Since the basic principle behind this line broadening mechanism is the same as for natural line broadening, it may be no surprise that this also results in a Lorentzian line profile.

The final line profile is of course a combination of all these broadening mechanisms. If we represent the natural line width by the function  $N(\lambda)$ , the thermal doppler broadening by  $G(\lambda)$  and the pressure broadening by  $P(\lambda)$ , we define the resulting line profile  $I(\lambda)$  as follows.

$$I(\lambda) = f(\lambda) \otimes N(\lambda) \otimes G(\lambda) \otimes P(\lambda) \quad (2.3)$$

This line profile is a convolution of the original line with all the broadening profiles. These profiles are a gaussian and two Lorentzians, which results in a Voigt line profile. This Voigt profile is characterized by a central gaussian with Lorentzian wings.

### 2.1.2 Measuring absorption lines

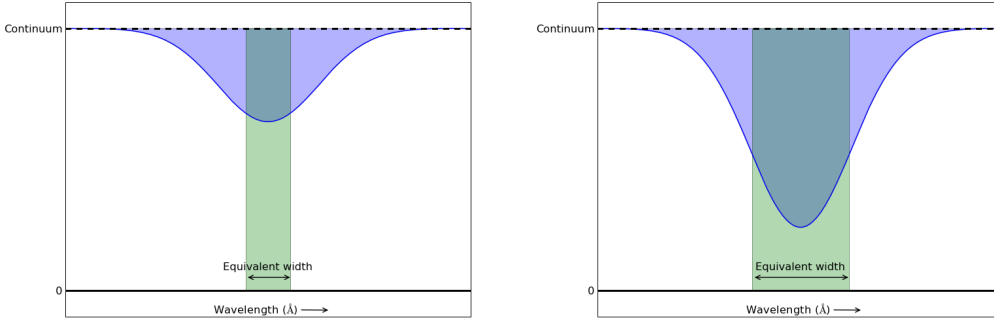
For this study, we needed a way to measure how strong an absorption line is. The best way to measure this strength is the equivalent width (EW) of an absorption line. The EW of a line tells you how wide the line would have to be to absorb the same amount of light with a line profile that is a block function instead of the profile described above. In other words, how broad would the line be if it were to absorb the same amount of light, but with total absorption instead of partial absorption. Figure 2.1 provides a visualization. In this figure, both the green and the blue regions have identical areas. For a more mathematical definition, we first define the total absorption as:

$$A = \int_{\lambda_{min}}^{\lambda_{max}} I_{cont}(\lambda) d\lambda - \int_{\lambda_{min}}^{\lambda_{max}} I(\lambda) d\lambda \quad (2.4)$$

where  $\lambda_{min}$  and  $\lambda_{max}$  are the boundaries of the absorption line. Now the equivalent width is defined to satisfy the next equation.

$$A = \int_{\lambda_0 - \frac{EW}{2}}^{\lambda_0 + \frac{EW}{2}} I_{cont}(\lambda) d\lambda \quad (2.5)$$

Figure 2.1: Two absorption lines with a different equivalent width



For EWs a theoretical curve of growth exists, which describes how the EW varies with temperature, metallicity and several other variables (Pagel, 1997). For this study, the most important aspect is that the relation between EW and the number of absorbing particles along the line of sight is roughly linear for most lines in the case of RGB-stars. Thus, this provides us with a very nice tool to investigate the dependence of spectral lines on other parameters. However, we do not know the exact number of particles, we only know it in relation to that of the Sun. This is because the metallicity, also denoted as  $[\text{Fe}/\text{H}]$  is defined as:

$$[\text{Fe}/\text{H}] = \log \frac{(N_{\text{Fe}}/N_{\text{H}})_{\star}}{(N_{\text{Fe}}/N_{\text{H}})_{\odot}} \quad (2.6)$$

One important aspect to consider when measuring absorption lines in spectra is the effect of line blending. Line blending occurs when two lines are so close to one another, that they overlap. At some point the two separate lines are indistinguishable from each other, which means that it is impossible to measure an accurate value of the equivalent width for either line.

## 2.2 The modeling of the spectra

We used synthetic spectra to model our data that were calculated with the program TurboSpectrum (Alvarez and Plez, 1998). This program uses a database of spectral lines to compute a spectrum based on the conditions in a given stellar atmosphere. The properties of these lines are taken from the Vienna Atomic Line Database (VALD) (Kupka et al., 1999). In Figure 2.2, we see a spectrum calculated with TurboSpec together with a real spectrum from the star Scl-31-11. The physical parameters of the model and the real star do not match completely, as can be seen in the width of the absorption line.

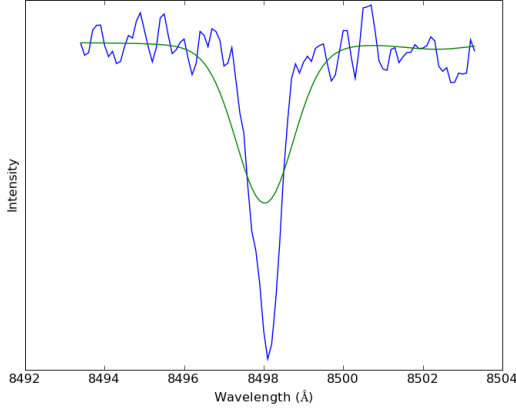


Figure 2.2: The simulated absorption line of Ca I 8498.38 Å compared to the one in a spectrum obtained with X-shooter. Both spectra are renormalized and the real spectrum is corrected for redshift.

The properties of a stellar atmosphere are calculated with the MARCS stellar model (Gustafsson et al., 2008), which has its origins in the 1970’s. Over the years it has undergone some significant changes, but the basics are still the same. First we will discuss the model and the basic assumptions it uses. After that we will explore what errors these assumptions might cause in the resulting synthetic spectra.

### 2.2.1 Basic assumptions

The MARCS stellar model is a classical model, in the sense that it is a one-dimensional model (Gustafsson et al., 2008). It can either be spherically symmetric or plane-parallel. Three-dimensional effects, such as rotation, have not been included.

With the assumption of spherical symmetry, the equation of hydrostatic equilibrium becomes

$$\nabla P_{tot} = -\rho \frac{GM_r}{r^2} \quad (2.7)$$

where  $M_r$  constitutes the mass within a certain radius  $r$ ,  $P_{tot}$  is the total pressure and  $\rho$  is the density. The MARCS model neglects the mass of the atmosphere, so for the atmosphere  $M_r = M$  is assumed to be true.

The gradient in the total pressure is given by the sum of the gradients of the gas pressure, the turbulent pressure and the radiative pressure (2.8). The radiative pressure is due to both absorption and scattering and is derived from the radiative transfer equation, leading to equation (2.9).

$$\nabla P_{tot} = \nabla P_{gas} + \nabla P_{turb} + \nabla P_{rad} \quad (2.8)$$

$$\nabla P_{rad} = -\frac{1}{c} \int_0^\infty (\kappa_\lambda + \sigma_\lambda) F_\lambda d\lambda \quad (2.9)$$

For the gas pressure, the ideal gas law ( $P_{gas} = R\rho T/\mu_{mol}$ ) is used where the variation in  $T$  and  $\mu_{mol}$  is neglected, so the gas pressure depends solely on the density.

The turbulence pressure is given as  $P_{turb} = \beta\rho v_t^2$ , where  $v_t$  is the characteristic turbulence velocity and  $\beta$  a correction factor roughly equal to 1. The value may vary, depending on whether the turbulent motions are more or less isotropic. For most of the lines, the turbulence pressure does not make a huge difference, but for the strong lines it is important. In our models, we used  $v_t = 2\text{km s}^{-1}$ , which is the expected mean for RGB-stars (Barklem et al., 2005).

The models do include convection as a means of energy transport, where the total energy flux is assumed to be the sum of the radiative and the convective flux (2.10). The convective flux is given by equation (2.11). This expression comes from the mixing length theory as described in Henyey et al. (1965).

$$F(r) = F_{\text{rad}}(r) + F_{\text{conv}}(r) \quad (2.10)$$

$$F_{\text{conv}} = \frac{1}{2} \rho C_p T v_{\text{conv}} \frac{l}{H_p} \delta\Delta \quad (2.11)$$

In this approach, one has certain liberties. The mixing length parameter  $\alpha = l/H_p$  can be chosen from a certain range of values. In these models,  $\alpha$  was set at 1.5, but other values can be chosen as well, changing the efficiency of convection.

Another assumption used is that local thermal equilibrium (LTE) applies everywhere. This implies that the Saha-equation is valid and that the Boltzmann equation can be used to calculate partition functions and excitation equilibria everywhere. An other implication of this assumption is that each layer of a star behaves like a blackbody. That gives us the following source function for radiative transfer.

$$S_\lambda = \frac{\kappa_\lambda}{\kappa_\lambda + \sigma_\lambda} B_\lambda(T) + \frac{\sigma_\lambda}{\kappa_\lambda + \sigma_\lambda} J_\lambda \quad (2.12)$$

### 2.2.2 Model errors

The assumptions that are made when constructing stellar models are necessarily an approximation of the real situation. This will therefore cause errors in the calculations made for the models. The two biggest assumptions are:

- $M_r = M$
- LTE applies everywhere throughout the model.

Looking at the atmosphere of the sun, it is only  $\approx 5 \times 10^{-4} R_\odot$  deep (Zeilik and Gregory, 1998), and considering that the densities at the surface are much lower than in the centre of the star, the mass contribution is very little. Add to that that  $M_r$  is only used linearly, and it is easy to see that this assumption will not cause major problems. The assumption of LTE is certainly not valid, because otherwise there would be no net energy flux through the atmosphere, which would prevent the stars from shining (Salaris and Cassisi, 2005). So there must be a slight asymmetry to allow stars to shine. Luckily, the asymmetry is very small. For the sun it is in the order of  $\approx 10^{-13}$ , but for the RGB stars studied here it can make a difference, especially when looking at the strong lines,

e.g. Starkenburg et al. (2010). However, calculating every line in non-LTE conditions is computationally unfeasible for this project. Additionally, one needs much better atomic models for these calculations and for a lot of atoms these models do not exist. For these reasons we stuck to LTE-models for our calculations.

Obviously, our assumptions are not valid. However, the errors are either very small or a better approximation is computationally unfeasible, so the advantages of a better calculation do not outweigh the extra efforts.

## 2.3 X-shooter

The X-shooter spectrograph is a new instrument for the Very Large Telescope (VLT) in Chile, built by an international consortium of institutes from France, Denmark, Italy, Germany and the Netherlands. With a large wavelength range from 3,000 to 25,000 Å, it will be useful for stellar spectroscopy, even though its spectral resolution is relatively low. X-shooter has an operational resolution between 4,000 and 14,000, depending on the wavelength region and the slit width. For detailed studies of stellar spectra this is rather low. A typical instrument for stellar high-resolution abundance studies is the UVES spectrograph, which has a maximum resolution of approximately 110,000 and has a wavelength range from 3,000 - 11,000 Å (Dekker et al., 2000).

The wavelength range and resolution of X-shooter are an unusual combination for stellar spectroscopy, and thus we will explore its characteristics and determine the value of X-shooter in comparison to other instruments.

X-shooter covers a long wavelength range from 3,000 to 25,000 Å with a single exposure. To be able to cover this large range, the instrument is divided in three arms, namely a UV-blue arm, a visual-red arm and a near-IR arm (D’Odorico et al., 2006). The overlap regions of these arms are at 5,500 Å and 10,000 Å. The arms do have their own instrumental characteristics, but these do not differ dramatically.

The spectral resolution at which the instrument operates for a reasonable slit width generally lies in the range of  $R = 4,000 - 14,000$ , where  $R$  is defined as:

$$R = \frac{\lambda}{\Delta\lambda} \quad (2.13)$$

and it depends on the wavelength region being considered and the slit width used during the observations. This resolution matters, because it defines the width of the gaussian with which all the spectral lines will be convolved, leading to a so-called instrumental broadening. This broadening will cause the disappearance of very narrow lines and might blend stronger lines together.

However, for the same star a lower resolution allows a higher signal-to-noise ratio (S/N) in the same exposure time than higher resolutions and this can be important for faint stars. To understand how this works, one has to keep in mind that the S/N increases with the number of photons that fall on a CCD-pixel. If the resolution is increased, each pixel covers a smaller wavelength region. For a constant spectral energy density, the amount of light caught per pixel decreases, and so does the S/N. To compensate for this loss of S/N, one can either increase the effective area of the telescope, i.e. use a mirror

with a larger surface area, or observe for a longer period of time.

So the loss of spectral resolution can be compensated for by a higher S/N, which allows fainter objects to be observed.

Summarizing, X-shooter combines a large wavelength range with a resolution suitable to observe faint objects, such as individual stars that are far away.

The primary goal of this project was to search for new absorption lines that could be detected with X-shooter and compile an overview of useful lines over the whole wavelength region. We wanted to study the behavior of these absorption lines for metal poor RGB stars, which are typically observed in nearby dwarf galaxies.

We created a grid of synthetic stellar spectra to cover the corresponding parameter space. All we had to do was find the useful absorption lines. In this particular case, that meant lines that can be detected and accurately measured with X-shooter, which implies that they should conform to a few conditions:

1. The line has to be strong enough, otherwise it disappears in the noise and the lack of resolution.
2. The line should not be severely blended. Blending makes it harder, if not impossible, to establish an accurate equivalent width for an individual line. This effect is a major problem for low-resolution stellar spectra.

It is particularly hard to check whether or not a line is blended in an automated fashion. It was therefore easier to do the selection by hand. However, going through the entire model grid by hand would take too much time, so we decided to select lines from an X-shooter spectrum of Scl-31-11. Scl-31-11 is a metal-poor RGB star with  $T_{eff}$ ,  $[Fe/H]$  and  $\log g$  that are quite average compared to the model grid. Therefore, the parameter values of this spectrum were a logical starting point. For the search of new lines, we only looked at the red part (5500–10,000 Å) of the spectrum. These VRI-bands are relatively unexplored and thus full of uncatalogued lines, unlike the UB-bands.

Twenty separate single-element spectra were generated and each one was manually searched for promising lines. For the UB bands we used a high-resolution linelist from Cayrel et al. (2004). After these steps, the entire model grid including all the lines considered was synthesized. We used a special spectral interpolation routine developed by T. Masseron to extend the parameter space of our model grid to the one used in Starkenburg et al. (2010) as shown in Table 3.1. Then we measured the EW of every

Table 3.1: The Full Parameter space

[Fe/H]	$[\alpha/\text{Fe}]$	$T_{eff}$	$\log g$
MARCS model atmospheres			
-0.25	+0.0, +0.1	3800, 3900, 4000, 4250, 4500, 4750, 5000	0.5, 1.0, 1.5, 2.0, 2.5
-0.50	+0.0, +0.2	3800, 3900, 4000, 4250, 4500, 4750, 5000	0.5, 1.0, 1.5, 2.0, 2.5
-0.75	+0.0, +0.3	3800, 3900, 4000, 4250, 4500, 4750, 5000	0.5, 1.0, 1.5, 2.0, 2.5
-1.00, -1.50, -2.00	+0.0, +0.4	3800, 3900, 4000, 4250, 4500, 4750, 5000	0.5, 1.0, 1.5, 2.0, 2.5
-2.50, -3.00	+0.4	3800, 3900, 4000, 4250, 4500, 4750, 5000	0.5, 1.0, 1.5, 2.0, 2.5
-4.00, -5.00	+0.4	3800, 3900, 4000, 4250, 4500, 4750, 5000	1.0, 1.5, 2.0, 2.5
Interpolated model atmospheres			
-1.25, -1.75		4125, 4375, 4625, 4875	0.75, 1.25, 1.75, 2.25
-2.25, -2.75		4125, 4375, 4625, 4875	0.75, 1.25, 1.75, 2.25
-3.50, -4.50		4125, 4375, 4625, 4875	1.25, 1.75, 2.25

absorption line in the entire parameter space of our model grid using an automatic program developed by Mike Irwin (Irwin, 2010).

Since this research project was particularly focused on the application to RGB-stars, we did not want to go through all the possible stars. Therefore we used the Yonsei-Yale isochrones (Kim et al., 2002) to pick out those combinations of  $\log g$  and  $T_{eff}$  that correspond to RGB-stars. This resulted in plots in which the equivalent width is plotted against metallicity for several values of the temperature (and the corresponding value of  $\log g$ ). An example for the CaI absorption line at 6162.17 Å can be found in Figure 3.1.

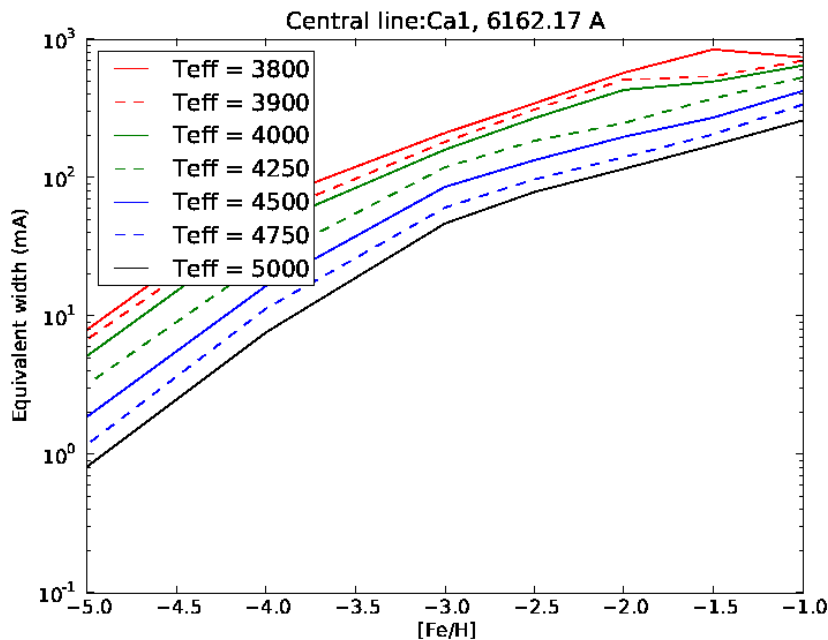


Figure 3.1: The dependence of EW on metallicity ( $[\text{Fe}/\text{H}]$ ) for the Ca 6162.17 Å absorption line over the range of  $T_{eff}$ -values expected for RGB-stars

Table 3.2: Label Assignment

Value	Label
$x_i < \mu_i - \sigma_i$	Low
$\mu_i - \sigma_i \leq x_i < \mu_i + \sigma_i$	Medium
$x_i \geq \mu_i + \sigma_i$	High

Figure 3.1 shows a straight line in a plot with a logarithmic Y-axis. Hence, an exponential can be fitted through this line. Using the relation in equation (3.1) and a fitting procedure, it was possible to determine the coefficient  $\alpha$  that determines the metallicity dependence.

$$EW = A \exp(\alpha [Fe/H]) \quad (3.1)$$

This gives an estimate of the metallicity dependence of the equivalent width of an absorption line. This procedure was followed for all the isothermal EW-relations, and the values of  $\alpha$  were averaged for each absorption line to get a representative value for every line. Since the difference in EW between two isothermal lines in Figure 3.1 remains almost constant with metallicity, the ratio of EW's of the two isotherms remains constant as well. Therefore, this ratio can serve as an indication of the temperature dependence. We looked at the temperature dependence in 3 regimes, namely low temperature, medium temperature and high temperature. For the low temperature, we calculated the EW-ratio for  $T_{eff} = 3800$  K and  $T_{eff} = 4000$  K for each metallicity, and then averaged the values. For the medium temperature we followed the same procedure, but with  $T_{eff} = 4000$  and 4500 K, and the ratios at high temperature were calculated with  $T_{eff} = 4500$  and 5000 K.

We now have a table with four dependences for each line, one on metallicity and three on  $T_{eff}$ . Since this might be hard to interpret, we give a more qualitative description. Therefore, for each dependence, we looked at the frequency of the values of this dependence. They followed a gaussian distribution, so we determined the mean and the standard deviation. The same procedure was followed for all four dependences, which resulted in a qualification of each dependence for every line.

Each parameter of each absorption line was then assigned the qualitative label 'Low', 'Medium' or 'High', according to Table 3.2.

For the important aspect of blending, we were able to put the absorption lines into three different classes. In the first, the line is not blended at all; the second case is severe blending, such that measuring an equivalent width is very difficult, if not impossible; the third case is intermediate, where blending only occurs at high metallicity.

The last check performed was to see whether an absorption line was very close to a telluric line, a strong absorption line from the terrestrial atmosphere. Telluric lines can make it difficult, if not impossible, to accurately measure the EW of a stellar absorption line, so it is very important to check that a stellar line is not too close to such a strong atmospheric absorption line. For this check, we used a telluric spectrum that was obtained with X-shooter.

Using the procedure described in the previous chapter, we have obtained detailed information about the characteristics of each stellar absorption line in our list. For each line we have the following information:

- The dependence on  $[\text{Fe}/\text{H}]$
- The dependence on  $T_{\text{eff}}$  over the range 3800 - 5000 K
- The minimum  $[\text{Fe}/\text{H}]$  required for a line to be detectable
- Whether the line is prone to blending with other lines
- The danger of blending with a telluric line

For the first two points we qualify the dependence as either weak, intermediate or strong. For the blending condition, we have two cases. If there is significant blending, we indicate that with a  $\zeta$ -mark. If there is only blending at higher metallicities, we use the  $\odot$ -sign.

These characteristics are all given for each stellar absorption line in Table 4.1. The lines are sorted alphabetically by element name, with increasing wavelength. To get a better idea of the distribution of lines with wavelength, one can have a look at Figure 4, where all lines are indicated based on wavelength and element. Newly found lines are typed boldface in Table 4.1

We found 17 new lines from several elements, such as Ba, Mg and Ti. These lines all have a wavelength larger than 5500 Å.

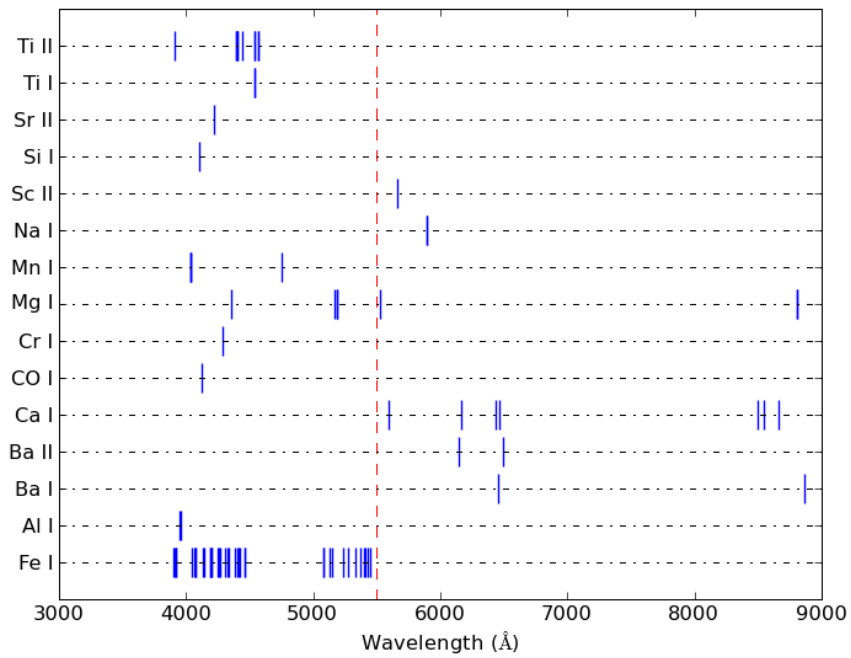


Figure 4.1: The linelist we determined for X-shooter spectra, sorted by element. The vertical dashed line indicates the transition from one spectral arm to the other.

Table 4.1: Feasible absorption lines and a qualitative description of their behavior in the X-shooter spectrograph

Element and Line	[Fe/H]-dep. <sup>1</sup>	T-dep. (Low $T_{eff}$ ) <sup>2</sup>	T-dep. (Medium $T_{eff}$ ) <sup>3</sup>	T-dep. (High $T_{eff}$ ) <sup>4</sup>	$[Fe/H]_{tres}$ <sup>5</sup>	Blending <sup>6</sup>	Telluric Lines
All 3943.90	Medium	Medium	High	Medium	< -5.0	☉	yes
All 3961.64	Medium	High	High	High	< -5.0	✗	yes
<b>BaI 6450.85</b>	High	Medium	High	High	-1.9	✗ / Nonexistent	
<b>BaI 8860.99</b>	High	Low	Low	Low	-1.8	✗ / Nonexistent	*
<b>BaII 6141.76</b>	Low	Low	Low	Medium	-1.4	✗	
<b>BaII 6496.90</b>	High	Medium	Medium	Medium	-4.0	✗	
<b>CaI 5588.75</b>	Medium	Medium	Medium	Medium	-4.1	✗	
<b>CaI 6162.17</b>	High	High	High	Medium	-2.9	✗	
<b>CaI 6439.08</b>	Medium	Medium	Medium	Low	-2.3		
<b>CaI 6462.58</b>	Medium	Medium	Medium	Medium	-2.8		
<b>CaI 8498.38</b>	Medium	Low	Low	Low	< -5.0		*
<b>CaI 8542.07</b>	Medium	Low	Low	Low	< -5.0		*
<b>CaI 8662.29</b>	Medium	Low	Low	Low	< -5.0		*
COI 4121.36	Low	High	Low	Medium	< -5.0	✗	yes
CrI 4289.93	Low	High	High	Low	-3.7	✗	
MgI 4352.62	Medium	High	High	High	-4.3	✗	yes
MgI 5172.49	Medium	Medium	Medium	Medium	< -5.0	✗	
MgI 5183.45	Medium	Medium	Medium	Medium	< -5.0		
<b>MgI 8806.76</b>	High	Low	Low	Low	-3.3	☉	*
<b>MgI 5528.41</b>	High	Medium	Medium	Medium	-1.6	✗	
MnI 4030.76	Medium	High	High	High	< -5.0	☉	yes
MnI 4033.28	Medium	High	High	High	< -5.0	✗	yes
MnI 4034.61	Medium	High	High	High	< -5.0	✗	yes
MnI 4753.67	Medium	High	High	High	-0.5		
<b>NaI 5889.95</b>	Medium	High	High	Medium	-4.5		
<b>NaI 5895.92</b>	High	High	High	Medium	-4.2		
<b>ScII 5657.90</b>	High	Low	Medium	Medium	-2.5	✗ / Nonexistent	
SiI 4103.63	Low	Low	Low	Low	< -5.0	✗ / Nonexistent	yes
SrII 4215.74	Medium	Medium	Low	Low	-4.5	✗	
<b>TiI 4536.14</b>	Low	High	High	High	< -5.0	✗	
TiII 3913.77	Low	Low	Low	Medium	-0.9	✗	yes

Element and Line	[Fe/H]-dep. <sup>1</sup>	T-dep. (Low $T_{eff}$ ) <sup>2</sup>	T-dep. (Medium $T_{eff}$ ) <sup>3</sup>	T-dep. (High $T_{eff}$ ) <sup>4</sup>	$[Fe/H]_{tres}$ <sup>5</sup>	Blending <sup>6</sup>	Telluric Lines
TiII 4394.80	Medium	Low	Low	Medium	-3.9	?	
TiII 4400.03	Medium	Medium	Low	Medium	-2.8	?	
TiII 4443.70	Medium	Low	Low	Low	-4.7	?	
TiII 4534.22	Medium	High	Medium	Medium	< -5.0	?	
TiII 4572.05	Medium	Medium	Medium	Medium	-4.2	?	
FeI 3902.93	High	Medium	High	High	< -5.0	?	yes
FeI 3906.28	High	Medium	Medium	Low	-4.8	?	yes
FeI 3920.11	High	High	High	High	< -5.0	?	yes
FeI 3922.89	Medium	High	High	High	-3.6	?	yes
FeI 4045.66	Medium	Medium	Medium	Medium	< -5.0	?	yes
FeI 4063.81	High	Medium	Medium	Medium	-4.7	?	yes
FeI 4071.79	Medium	Medium	Medium	Medium	-4.8	?	yes
FeI 4076.61	Low	High	High	High	< -5.0	?	yes
FeI 4131.83	Medium	Medium	High	High	-4.6	?	yes
FeI 4143.85	High	Medium	Medium	Medium	-4.3	?	yes
FeI 4186.64	Medium	Medium	High	Medium	-4.4	?	yes
FeI 4188.10	Medium	Medium	Medium	High	-4.5	?	yes
FeI 4199.74	High	Medium	High	High	-3.4	?	yes
FeI 4201.99	High	Medium	Medium	High	-3.3	?	
FeI 4250.82	Medium	Medium	Medium	Medium	< -5.0	?	
FeI 4260.44	High	Medium	High	Low	-3.0	?	
FeI 4271.99	Medium	High	Medium	Medium	-4.6	?	
FeI 4307.77	Low	Low	High	High	< -5.0	?	
FeI 4325.84	Medium	Low	High	High	< -5.0	?	yes
FeI 4337.07	Medium	High	Low	Low	< -5.0	?	yes
FeI 4383.39	Medium	Medium	Medium	Medium	< -5.0	?	yes
FeI 4404.74	Medium	Medium	Medium	High	-4.6	?	
FeI 4415.11	Medium	Medium	Low	Low	-4.0	?	
FeI 4427.28	Low	High	Medium	Medium	-3.4	?	
FeI 4458.96	High	High	High	High	-1.8	?	
FeI 4461.86	Medium	High	High	High	-3.6	?	
FeI 5079.55	High	Medium	High	High	-3.9	?	
FeI 5083.59	Medium	High	High	High	-2.9	?	
FeI 5127.74	High	Medium	High	High	-3.1	?	

Element and Line	[Fe/H]-dep. <sup>1</sup>	T-dep. (Low $T_{eff}$ ) <sup>2</sup>	T-dep. (Medium $T_{eff}$ ) <sup>3</sup>	T-dep. (High $T_{eff}$ ) <sup>4</sup>	$[Fe/H]_{tres}$ <sup>5</sup>	Blending <sup>6</sup>	Telluric Lines
FeI 5150.69	Medium	High	High	High	-3.4	⚡	
FeI 5232.74	Low	High	Medium	Medium	-3.0	⊙	
FeI 5269.52	Medium	Medium	Medium	Medium	< -5.0	⚡	
FeI 5327.98	Medium	Medium	Medium	Medium	< -5.0	⊙	
FeI 5371.29	Medium	Medium	Medium	Medium	-4.4	⊙	
FeI 5396.94	Medium	Medium	Medium	Medium	-4.0	⊙	
FeI 5405.72	Medium	Medium	Medium	Medium	-4.6		
FeI 5429.70	Medium	Medium	Medium	Medium	-3.7	⚡	
FeI 5446.47	Medium	Medium	High	High	-3.6	⊙	

<sup>1</sup>The index  $\alpha$  in the dependence  $EW = ae^{\alpha[Fe/H]}$ , bin limits are 0.31 and 0.60

<sup>2</sup>The average of the EW-ratio at  $T = 3800$  and  $T = 4000$ :  $< \frac{EW_{4000}}{EW_{3800}} >$ , bin limits are 1.10 and 1.38

<sup>3</sup>Idem, but now with  $T = 4000$  and  $T = 4500$ , bin limits are 1.59 and 2.04

<sup>4</sup>Idem, but now with  $T = 4500$  and  $T = 5000$ , bin limits are 1.64 and 2.17

<sup>5</sup>The value of [Fe/H] for which, at  $T = 4500$  K, the EW exceeds the detectability threshold

<sup>6</sup>A ⚡-mark indicates a possibility of blending, a ⊙-mark indicates blending only at higher [Fe/H].

This project encountered several sources of errors that required careful handling. They will be discussed, together with their origin and the impact on the results, in section 5.1. In section 5.2 we will discuss the results we found and their implications.

## 5.1 Sources of Error

An important part of every research project is to consider the effect of errors on the analysis. The errors we encountered during the project arose especially when creating the synthetic spectra and during the analysis of the equivalent widths of every absorption line. The errors from the synthesis of the spectra will be discussed in section 5.1.1, while the errors in the analysis are discussed in section 5.1.2.

### 5.1.1 Errors in Creating Synthetic Spectra

The synthetic spectra are calculated from a sequence of models. First, a program calculates the physical parameters of the stellar atmosphere from which the lines originate. Then a different program calculates for every absorption line how it is affected by these parameters, building up a realistic spectrum. The errors in this process, which are discussed in detail in section 2.2.2, follow from the assumptions made to simplify the stellar models. The two basic assumptions used are:

1. Throughout the entire atmosphere, the mass within a given radius equals the total mass of the star,  $M_r = M$ . Careful analysis shows that this approximation does not cause severe problems, because the atmosphere has a mass contribution of only  $\approx 10^{-4}M_\star$ . Furthermore,  $M_r$  is only used in a linear fashion, so the errors are minimal, and typically negligible.
2. Local thermal equilibrium (LTE) applies in the stellar atmosphere. This is not an entirely valid assumption, since complete thermal equilibrium would mean that a star would not radiate. However, the asymmetry is of order  $\approx 10^{-13}$ , so this is a very small error and can probably be neglected for most lines.

So, in conclusion there are errors in our stellar models and the assumptions we use to create synthetic spectra, but they are all small enough not to have a significant impact on our analysis and results.

### 5.1.2 Equivalent Widths

While dealing with the EW measurements, we encountered two major sources of error. The first is that the curve of growth, the relation between EW and  $[\text{Fe}/\text{H}]$ , is not always an exponential as it turns over at higher values of  $[\text{Fe}/\text{H}]$ . Secondly, the measurements including the errors do not precisely follow the relation, but have a scatter around it. This scatter is larger for lines with smaller equivalent widths. If not properly understood and taken into account, these errors can lead to biased conclusions.

1. At higher metallicities the EW vs.  $[\text{Fe}/\text{H}]$  plots exhibit a cutoff in the exponential trend at the point they reach the horizontal plateau of the curve of growth. This is where the EW no longer increases with metallicity. This cutoff skews our assesment of the metallicity-dependence towards a weaker dependence. The turnoff happens for all lines at approximately the same metallicity ( $[\text{Fe}/\text{H}] \approx -1.5$ ), so the effect is more or less comparable for every line. Since we studied the metallicity-dependence only in relation to other lines, and because the effect on every line is comparable, the influence of this effect on our results is limited.
2. Unfortunately, not all EW vs.  $[\text{Fe}/\text{H}]$  plots showed the nice, straight lines seen in figure 3.1. This is particularly true for lines with small equivalent widths. This is most likely caused by the large relative error in the measurement of the EW of these lines. This error can only be reduced with more accurate EW's, which can be achieved with a higher spectral resolution.

## 5.2 Results

We achieved several results with this project. First, we were able to study and qualify the behavior of tens of common optical absorption lines for RGB stars and put all this information together in a single table. This table can be a useful tool for observers in the future to check their spectrum for these lines. Additionally, we added absorption lines of other elements, such as Ba and Na to the list, providing an even more comprehensive table of absorption line characteristics than was previously available. The most significant result is the extension of the table to include lines from the red part of the spectrum. This spectral region is relatively unexplored and one of the reasons why it is so unexplored is that there are fewer lines. This lack of lines has an advantage: it lowers the possibility of blending, which is necessary for analysing stellar spectra with relatively low resolution spectrographs like X-shooter. Since X-shooter has a large wavelength range, it is the ideal instrument to explore this spectral regime. This long wavelength coverage also means that new lines can be compared to traditional lines at a bluer wavelength.

In this study we presented an overview of absorption lines that can be used for spectral analysis of RGB-stars with X-shooter. Exploring synthetic spectra proved to be a good method to search for these absorption lines. Although the selection of a linelist of detectable lines still had to be done by hand, the rest of our calculations were completely automated. This makes it very easy to expand the study and incorporate new lines. The automated calculations provide a reliable indication of the relative dependence of the equivalent width of a line on  $[\text{Fe}/\text{H}]$  and  $T_{\text{eff}}$ . In addition to the dependences we also give an indication whether a line is prone to blending with another absorption line or a telluric line. We used a telluric spectrum obtained with X-shooter for this last check.

We expanded the search for absorption lines to include lines with a wavelength up to 10,000 Å, a relatively unexplored wavelength regime. Additionally, we included some lesser-used elements in that search to increase the number of feasible lines. We studied these lines together with already known lines and then put it all together in a single table. This table provides a good tool for observers to check their spectra for the more common stellar absorption lines when studying metal-poor RGB-stars.

Of course we encountered the problem of assumption in our calculations that are not correct. We investigated the assumptions of applicability of Local Thermal Equilibrium and  $M_r = M_*$  throughout the stellar atmosphere and they turn out not to cause major problems, so we neglected these sources of error. Other errors in the handling of the EW's do not cause severe problems within this project, but further research is recommended to find a more complete solution to this issue.

The resulting table will be applied in the study of extremely metal-poor stars in dwarf galaxies, but this is of course just a start. One could expand this list for the red regime with lines from more metal-rich stars, or use stars other than RGB-stars.

## CHAPTER 7

### ACKNOWLEDGEMENTS

This project would not have been possible without the help of many people. First of all, I would like to thank my supervisors Eline Tolstoy and Else Starckenburg for their invaluable support. Their help and suggestions really helped me back on track when I got lost.

Many thanks go out to the other people in the Eline Tolstoy's research group, who always gave me useful hints and suggestions during and outside of the group meetings.

I am also very grateful for the linelist Vanessa Hill provided me with and for the EW-measuring routine created by Mike Irwin.

Furthermore, I owe a lot to the students of the Kapteyn Astronomical Institute, who always helped me with all my questions and problems that arose during the project. Last but not least, I would like to thank my family, friends and housemates for giving me an almost endless amount of support and coffee to finish this project.

## BIBLIOGRAPHY

- Alvarez, R. and Plez, B. (1998). Near-infrared narrow-band photometry of M-giant and Mira stars: models meet observations. *Astronomy & Astrophysics*, 330:1109–1119.
- Barklem, P. S., Christlieb, N., Beers, T. C., Hill, V., Bessell, M. S., Holmberg, J., Marsteller, B., Rossi, S., Zickgraf, F., and Reimers, D. (2005). The Hamburg/ESO R-process enhanced star survey (HERES). II. Spectroscopic analysis of the survey sample. *Astronomy & Astrophysics*, 439:129–151.
- Cayrel, R., Depagne, E., Spite, M., Hill, V., Spite, F., François, P., Plez, B., Beers, T., Primas, F., Andersen, J., Barbuy, B., Bonifacio, P., Molaro, P., and Nordström, B. (2004). First stars V - Abundance patterns from C to Zn and supernova yields in the early Galaxy. *Astronomy & Astrophysics*, 416:1117–1138.
- Dekker, H., D’Odorico, S., Kaufer, A., Delabre, B., and Kotzlowski, H. (2000). Design, construction, and performance of UVES, the echelle spectrograph for the UT2 Kueyen Telescope at the ESO Paranal Observatory. In M. Iye & A. F. Moorwood, editor, *Society of Photo-Optical Instrumentation Engineers (SPIE) Conference Series*, volume 4008 of *Society of Photo-Optical Instrumentation Engineers (SPIE) Conference Series*, pages 534–545.
- D’Odorico, S., Dekker, H., Mazzoleni, R., Vernet, J., Guinouard, I., Groot, P., Hammer, F., Rasmussen, P. K., Kaper, L., Navarro, R., Pallavicini, R., Peroux, C., and Zerbi, F. M. (2006). X-shooter UV- to K-band intermediate-resolution high-efficiency spectrograph for the VLT: status report at the final design review. In *Society of Photo-Optical Instrumentation Engineers (SPIE) Conference Series*, volume 6269 of *Society of Photo-Optical Instrumentation Engineers (SPIE) Conference Series*.
- Gustafsson, B., Edvardsson, B., Eriksson, K., Jørgensen, U. G., Nordlund, Å., and Plez, B. (2008). A grid of MARCS model atmospheres for late-type stars. I. Methods and general properties. *Astronomy & Astrophysics*, 486:951–970.
- Heney, L., Vardya, M. S., and Bodenheimer, P. (1965). Studies in Stellar Evolution. III. The Calculation of Model Envelopes. *The Astrophysical Journal*, 142:841–+.
- Irwin, M. (2010). Private communication.

- Ivans, I. I., Kraft, R. P., Sneden, C., Smith, G. H., Rich, R. M., and Shetrone, M. (2001). New Analyses of Star-to-Star Abundance Variations among Bright Giants in the Mildly Metal-poor Globular Cluster M5. *Astronomical Journal*, 122:1438–1463.
- Kim, Y., Demarque, P., Yi, S. K., and Alexander, D. R. (2002). The  $Y^2$  Isochrones for  $\alpha$ -Element Enhanced Mixtures. *The Astrophysical Journal Supplement Series*, 143:499–511.
- Kupka, F., Piskunov, N., Ryabchikova, T. A., Stempels, H. C., and Weiss, W. W. (1999). VALD-2: Progress of the Vienna Atomic Line Data Base. *Astronomy & Astrophysics Supplement*, 138:119–133.
- McWilliam, A. (1997). Abundance Ratios and Galactic Chemical Evolution. *Annual Review of Astronomy & Astrophysics*, 35:503–556.
- Pagal, B. E. J. (1997). *Nucleosynthesis and Chemical Evolution of Galaxies*. Cambridge University Press.
- Salaris, M. and Cassisi, S. (2005). *Evolution of Stars and Stellar Populations*. John Wiley & Sons.
- Starkenburg, E., Hill, V., Tolstoy, E., González Hernández, J. I., Irwin, M., Helmi, A., Battaglia, G., Jablonka, P., Tafelmeyer, M., Shetrone, M., Venn, K., and de Boer, T. (2010). The NIR Ca ii triplet at low metallicity. Searching for extremely low-metallicity stars in classical dwarf galaxies. *Astronomy & Astrophysics*, 513:A34+.
- Tielens, A. G. G. M. (2005). *The Physics and Chemistry of the Interstellar Medium*. Cambridge University Press.
- Tolstoy, E., Hill, V., and Tosi, M. (2009). Star-Formation Histories, Abundances, and Kinematics of Dwarf Galaxies in the Local Group. *Annual Review of Astronomy & Astrophysics*, 47:371–425.
- Zeilik, M. and Gregory, S. (1998). *Introductory Astronomy and Astrophysics*. Harcourt College Publishers.